2012

Microstructure-property relationship in the thermomechanically processed C-Mn-Si-Nb-Al-(Mo) transformation-induced plasticity steels before and after prestraining and bake hardening treatment

I B. Timokhina
Deakin University, Ilana.Timokhina@eng.monash.edu.au

M Enomoto
Ibaraki University, Hitachi, Japan.

M K. Miller
Oak Ridge National Laboratory, Oak Ridge

E V. Pereloma
University of Wollongong, elenap@uow.edu.au

Publication Details

Timokhina, I. B., Enomoto, M., Miller, M. K. & Pereloma, E. V. (2012). Microstructure-property relationship in the thermomechanically processed C-Mn-Si-Nb-Al-(Mo) transformation-induced plasticity steels before and after prestraining and bake hardening treatment. Metallurgical and Materials Transactions A: Physical Metallurgy and Materials Science, 43 (7), 2473-2483.

Microstructure-Property Relationship in the Thermomechanically Processed C-Mn-Si-Nb-Al-(Mo) Transformation-Induced Plasticity Steels Before and After Prestraining and Bake Hardening Treatment

I.B. TIMOKHINA, M. ENOMOTO, M.K. MILLER, and E.V. PERELOMA

The effect of prestraining and bake hardening (PS/BH) on the development of microstructures and mechanical properties in thermomechanically processed transformation-induced plasticity (TRIP) steels with additions of Nb, Mo, and Al was studied by atom probe tomography (APT) and transmission electron microscopy (TEM). An increase in number density and sizes of clusters and nanoscale precipitates was observed in both steels but was more significant in the Nb-Al-Mo steel than in the Nb-Al steel. This increase could be explained by the possible fast diffusion of Nb and Mo atoms at low temperatures, as was observed for surface diffusivity. The contributions of cluster strengthening and precipitation strengthening to the yield strength increment after PS/BH were estimated.

DOI: 10.1007/s11661-012-1106-8

I. INTRODUCTION

THE increased demand worldwide for high strength steels for automotive applications is driven by the high oil prices, new emissions compliance regimes, and higher safety requirements. The higher strength product could offer equivalent strength at proportionally reduced thickness, and therefore reduced weight. Transformation-induced plasticity (TRIP) steel is a possible candidate for automotive applications, as they demonstrate a high ultimate tensile strength (~900 to 1100 MPa) without sacrificing ductility (30 to 40 pct).[1] There are two processing routes for TRIP steels: one involves cold rolling and intercritical annealing (IA), whereas the other is controlled by thermomechanical processing (TMP). The conventional composition of TRIP steels is Fe-0.15-0.2 wt pct C-1.5 wt pct Mn-1.5 wt pct Si with possible substitution of Si by Al or addition of Mo, Cu, and P.[2–5] The substitution of Si by Al is driven by the need for automotive sheet galvanizing, as high Si content degrades the adhesion of Zn by formation of a thin surface oxide layer. Mo increases the hardenability of steel and also assists its galvanizing.[4] Microalloying additions of carbide or carbo-nitride forming elements, such as Nb or Ti, are used for refinement of the microstructure and further strength increases.[6] Simultaneous additions of Nb and Mo lead to even further strength increases due to NbMoC precipitation hardening.[7,8]

The microstructure of a thermomechanically processed TRIP steel consists of polygonal ferrite (PF), bainite (B), retained austenite (RA), and possibly some martensite (M) or carbide-containing B, typically found in commercial alloys.[9] To a large extent, the properties of TRIP steels are determined by the interaction of the phases present in the microstructure, as well as by the stability of RA, which transforms continuously to M during straining.[10,11] This results in a localized increase of the strain-hardening coefficient that delays the onset of necking, leading to high elongation without compromising strength.[12]

During car manufacturing, the automotive body is formed, paint coated, and then baked at temperatures of 423 to 473 K (150 to 200 °C) for 20 to 30 minutes.[13] During this process, the steel is strain aged. This results in changes in microstructure and mechanical properties (*i.e.*, a yield strength increase). This leads to improved shape fixability, dent, and crash resistance.[13] Bake hardening (BH) is typically associated with the pinning of dislocations by atmospheres of solute atoms, such as carbon or nitrogen.[14] Research on the BH response of intercritically annealed TRIP steels showed that the maximum increase (100 MPa) was observed in TRIP steels after 2 to 10 pct prestraining (PS) followed by baking out at 443 to 448 K (170 to 175 °C) for 20 minutes.[13,15,16] The yield strength increase in intercritically annealed TRIP steels is accompanied by the appearance of the upper yield point due to the formation of Cottrell atmospheres around dislocations, a slight increase in the tensile strength, and a decrease in the elongation.[14] Contrarily, a study performed by the

I.B. TIMOKHINA, Senior Research Academic, is with the Centre for Material and Fibre Innovation, Deakin University, VIC 3216, Australia. Contact e-mail: ilanat@deakin.edu.au M. ENOMOTO, Professor, is with the Department of Materials Science and Engineering, Ibaraki University, Hitachi 316-8511, Japan. M.K. MILLER, Professor, is with the Microscopy Group, Materials Science and Technology Division, Oak Ridge National Laboratory, Oak Ridge, TN 37831-6136. E.V. PERELOMA, Professor, is with the School of Mechanical, Materials and Mechatronic Engineering, University of Wollongong, NSW 2522, Australia.

Manuscript submitted September 1, 2011.
Article published online March 20, 2012

authors on the BH of thermomechanically processed TRIP steels showed continuous yielding behavior and increases in both tensile strength and elongation.[17–19] This indicates the operation of different mechanisms in intercritically annealed and thermomechanically processed TRIP steels. Moreover, the additions of Al, Mo, and Nb to the composition on thermomechanically processed steels and the possible formation of carbides could also affect the BH behavior of these steels. The aim of this study was to understand how the microstructure of C-Mn-Si-Nb-Al-(Mo) steels before and after PS/BH treatment can influence the mechanical properties.

II. EXPERIMENTAL PROCEDURE

The compositions of two steels used in this study are given in Table I. Both steels were subjected to laboratory-simulated TMP. The TMP schedules were designed using the continuous cooling transformation data to form 50 pct of PF, noncarbide B with a maximum amount of RA. The TMP schedules included a reheat to 1523 K (1250 °C), a hold for 120 seconds, followed by hot rolling using a one-stand rolling mill to 25 pct reduction in the recrystallized (1373 K (1100 °C)) and 47 pct reduction in the nonrecrystallized (1148 K (875 °C)) austenite regions. After the second deformation, the steels were slowly cooled (1 Ks^{-1}) through the austenite to ferrite transformation region down to 1113 K (840 °C) for the Nb-Al and to 1033 K (760 °C) for Nb-Mo-Al steel to form ferrite, followed by water mist cooling at 20 Ks^{-1} to avoid pearlite formation. Then the steel plate was immediately transferred into a fluidized bed furnace at 743 K (470 °C) for 1200 seconds for the Nb-Al-Mo and at 773 K (500 °C) for 1800 seconds for Nb-Al steel to simulate coiling, during which formation of carbide-free B takes place, followed by quenching. After the TMP, the tensile samples were machined from the strips according to ASTM standard[20] and PS to 4 pct. Bake hardening was performed at 453 K (180 °C) for 1800 seconds. These parameters were chosen as the best response from a preliminary study on the effect of PS/BH conditions on the hardness of these steels.

Room temperature mechanical properties of the samples after TMP and TMP/BH were determined with an INSTRON* 4500 servohydraulic tensile testing machine with a 100 kN load cell. Four samples were tested for each condition. An increase in the yield stress due to the BH treatment was measured as the difference between the upper yield strength after treatment and the flow stress after PS.[21]

X-ray diffraction was performed with a PHILIPS** PW 1130 (40 kV, 25 mA) diffractometer to determine the amount of RA using the direct comparison method, a detailed description of which can be found elsewhere.[22,23]

The detailed characterization of the microstructure after TMP and PS/BH was performed with a PHILIPS CM 20 transmission electron microscope operated at 200 kV. Samples for transmission electron microscopy (TEM) analysis were cut perpendicular to the rolling direction. Thin foils were prepared by twin-jet electropolishing using 5 pct of perchloric acid in methanol at 248 K (–25 °C) at 50 V. The TEM replica technique was used to investigate the particles formed after TMP and PS/BH. Carbon replicas were collected on the Ni grids. Energy-dispersive X-ray spectroscopy (EDXS) was used to study the particle compositions. The dislocation density of PF before and after PS/BH was calculated using bright and dark TEM images at a magnification of 66,000 times by measuring the total dislocation line length in a unit volume of crystal.[24] The foil thickness for the calculation was determined from intensity oscillations in the two-beam convergent beam electron diffraction (CBED) patterns.

The local electrode atom probe experiments were performed at Oak Ridge National Laboratory. The samples for both steels were cut perpendicular to the deformation (rolling) direction. The atom probe specimens were prepared according to the standard two-stage electropolishing procedure.[25] Atom probe tomography (APT) was performed with a sample temperature of 60 K (–213 °C), a pulse repetition rate of 200 kHz, and a 0.2 pulse fraction. Background noise subtraction was used for determination of the composition of the matrix. The extent of solute-enriched regions (radius of gyration) and the local solute concentrations in these regions was estimated with the maximum separation envelope method with a grid spacing of 0.1 nm.[25] The Guinier radius, which represents the actual size of particles, was calculated from[25]

$$r_G = \sqrt{\frac{5}{3} l_g} \qquad [1]$$

*INSTRON is a trademark of Instron, Canton, MA.

**PHILIPS is a trademark of FEI Company, Hillsboro, OR.

Table I. Steel Compositions and Processing Parameters

	Element (At. Pct)								Parameters		
Steel	C	Si	Mn	Mo	Al	Cu	Nb	P	T_{AC} (°C)	T_{IH} (°C)	t_{IH} (s)
Nb-Al	1.00	2.31	1.52	0.002	1.15	0.026	0.022	0.048	840	500	1800
Nb-Al-Mo	0.95	2.29	1.51	0.17	1.15	0.026	0.021	0.048	760	470	1200

T_{AC}—accelerated cooling start temperature, T_{IH}—isothermal hold temperature, and t_{IH}—holding time.

where r_G is the Guinier radius and l_g is the radius of gyration.

The maximum separation distance, d_{max}, between the atoms of interest of 1 nm was used for the clusters in ferrite/bainitic ferrite, whereas the separation distance for clusters in M was $d_{max} = 0.5$ nm. A minimum of 20 atoms was accepted to define the small clusters in order to eliminate random fluctuations.[25]

III. RESULTS

A. *Mechanical Properties*

Both steels exhibit a good combination of strength and ductility, as well as continuous yielding behavior after TMP (Table II, Figure 1). However, the Nb-Al-Mo steel had better strength/ductility balance than the Nb-Al steel (Table II, Figure 1). After PS/BH treatment, a significant increase in yield strength was observed for both steels (Table II, Figure 1). The bake-hardening response for the Nb-Al steel was slightly lower (50 MPa) than for the Nb-Al-Mo steel (70 MPa) (Table II). It is important to note that the stress-strain curves for both steels after PS/BH still exposed the continuous behavior; *i.e.*, no yield point phenomenon was detected in any sample tested.

B. *TEM Characterization*

The detailed description of the microstructure of these steels after TMP is given elsewhere.[26] The microstructure of both steels after TMP consisted of ~50 pct PF, ~30 pct B, RA, and remaining M. The predominant B morphology for both steels was acicular ferrite, *i.e.*, the B that consists of bainitic ferrite laths with interlayers of austenite or M (Figures 2(a) and (b)). However, some amount of granular B, which is defined as equiaxed bainitic ferrite grains and M/austenite islands between them, was also found in the microstructure. The Nb-Al-Mo showed more refined bainitic ferrite laths compared to the Nb-Al steel (Figures 2(a) and (b)). The average dislocation density of PF was ~3.7×10^{14} m^{-2} in the Nb-Al-Mo steel and ~2×10^{14} m^{-2} in the Nb-Al steel. The volume fraction of RA determined by X-ray technique was 7 pct with the average carbon content of 3.17 at. pct C in the Nb-Al steel, and 12 pct with the average carbon content of 7.3 at. pct C in the Nb-Al-Mo steel.

TEM of the samples after PS/BH revealed an increase in the average dislocation density of PF grains to 7×10^{14} m^{-2} and 4.2×10^{14} m^{-2} for the Nb-Al and for the Nb-Al-Mo steels, respectively. The formation of cells and microbands was observed in PF of both steels in most of the cases in the vicinity or in between B or M (Figures 2(c) and (d)). Most of the M islands in studied steels contained twins (Figure 2(e)). After PS/BH, the RA volume fraction reduced to 8 pct in the Nb-Al-Mo steel, whereas practically all the RA present in the Nb-Al steel transformed to M. Fe_3C carbides were observed in the PF and bainitic ferrite of both steels after PS/BH (Figure 2(f)).

C. *Particle Characterization*

TEM study of particles was performed with a replica technique, as the high dislocation density of bainitic

Table II. Mechanical Properties of Steels

Steel	Processing	UTS (MPa)	YS (MPa)	Total El (Pct)	Uniform El (Pct)	Average BH Response (MPa)
Nb-Al	TMP	1040 ± 40	470 ± 30	29 ± 3	20 ± 2	—
	TMP/PS/BH	1041 ± 40	950 ± 10	25 ± 3	16 ± 2	50
Nb-Al-Mo	TMP	1153 ± 50	570 ± 30	35 ± 5	20 ± 2	—
	TMP/PS/BH	1168 ± 50	1030 ± 15	27 ± 4	11 ± 2	70

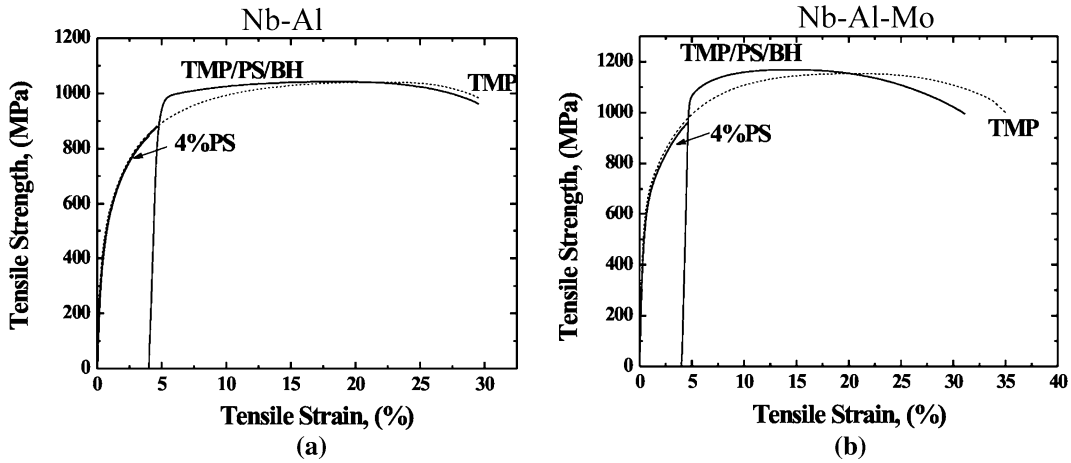

Fig. 1—Representative stress-strain curves of the (*a*) Nb-Al and Nb-Al-Mo steels after TMP and PS/BH.

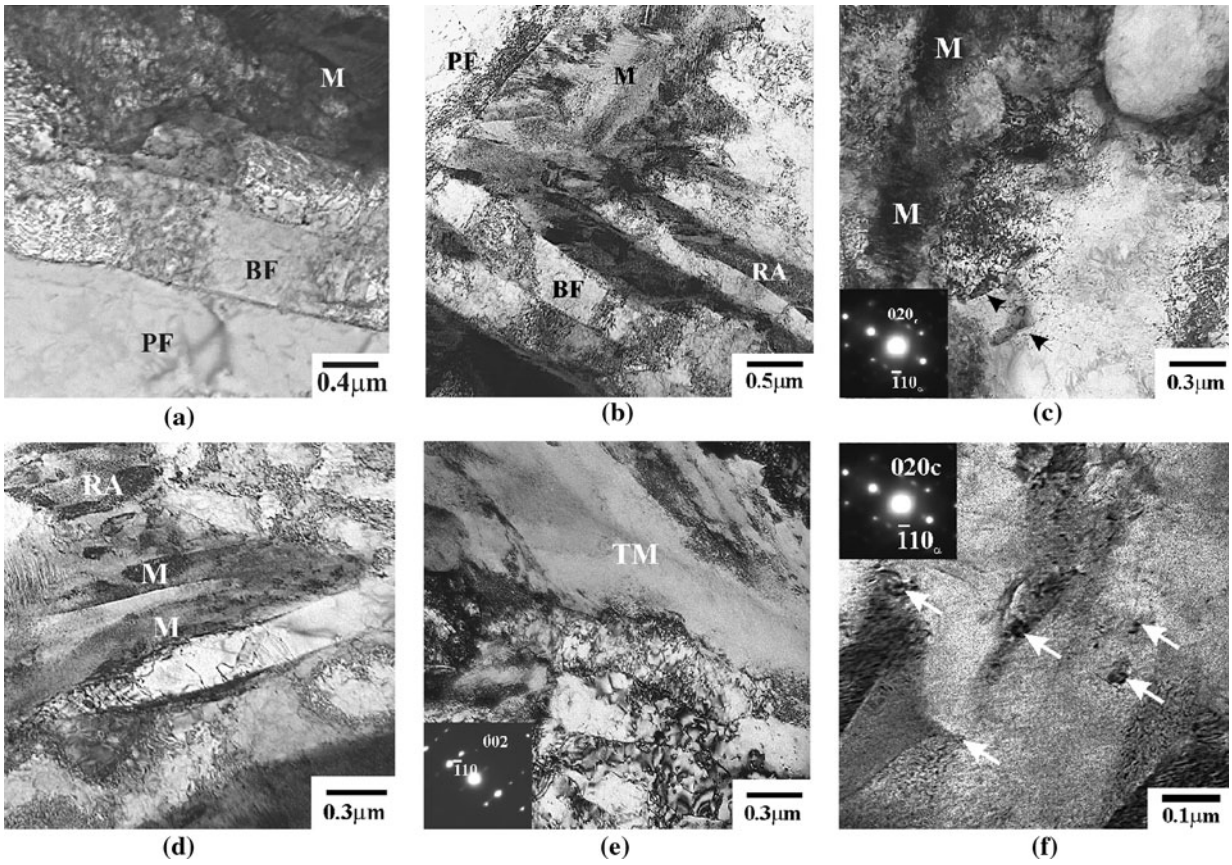

Fig. 2—TEM micrographs of (*a*) Nb-Al steel after TMP, (*b*) Nb-Al-Mo steel after TMP, (*c*) formation of cell structure and Fe_3C carbides indicated by arrows ($[111]_\alpha//[\bar{1}00]_c$) in PF of Nb-Al-Mo steel after PS/BH, (*d*) formation of microbands in PF between M crystals in Nb-Al steel after PS/BH, (*e*) M twinning in the Nb-Al-Mo steel (zone axis is $[110]_\alpha$, twin plane is (121) $_\alpha$) after PS/BH treatment, and (*f*) formation of Fe_3C carbides in B after PS/BH treatment in the Nb-Al-Mo steel (diffraction pattern (inset) is from carbide with a zone axis of $[\bar{1}00]$). PF is polygonal ferrite, BF is bainitic ferrite, M is martensite, RA is retained austenite, and TM is twined martensite. Arrows indicate carbides.

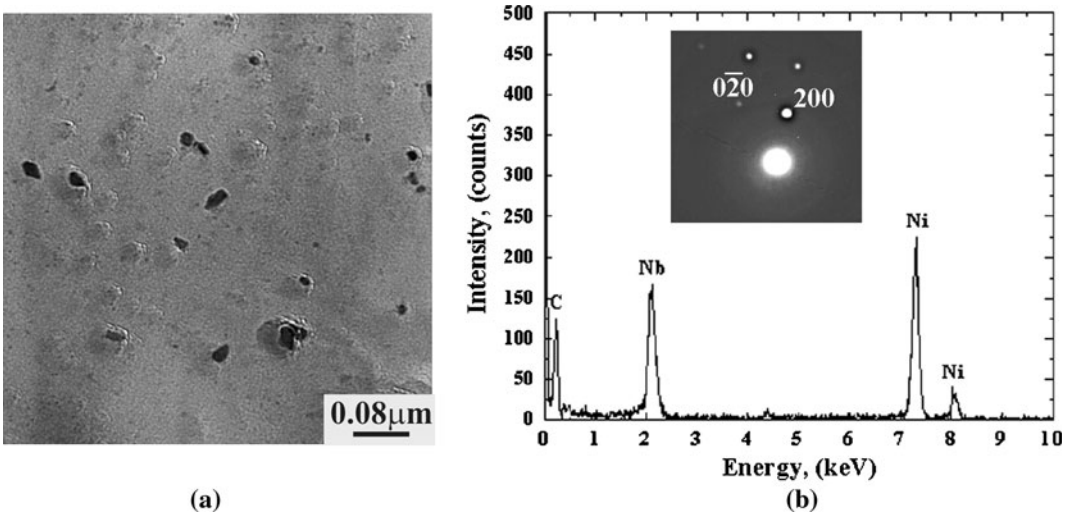

Fig. 3—(*a*) Carbon replica from the Nb-Al samples after TMP and (*b*) representative EDX spectrum and diffraction pattern with zone axis of $[001]_{NbC}$ (inset) from the NbC carbides. The Ni peak is from the Ni grid.

ferrite, for instance, makes particle analysis difficult with conventional TEM technique. The study of the replicas after TMP revealed the predominate formation of NbC with cubic lattice structure and lattice parameters of $a = b = c = 0.45$ nm in the Nb-Al steel (Figures 3(a) and (b)). The particles showed the cubelike and globular-like shapes. The cubelike Nb carbides were undissolved precipitated during austenitizing, whereas

globular-like Nb carbides might form during TMP. As the replica technique does not provide information on the microstructure, it was impossible to identify whether the particles were formed in ferrite or B. The carbides were uniformly distributed throughout the matrix within some areas, whereas other areas showed clustering of particles. However, it appeared that the particles that were less than ~2 nm in size were not extracted from the matrix and were not detected by this technique. The average size of fine particles after TMP was 14 ± 7 nm (Table III, Figure 4(a)). The number density of particles in the Nb-Al steel after PS/BH remained almost the same (Table III). The size of Nb carbides became coarser than after TMP (Table III, Figure 4(a)).

Analysis of EDXS spectra and indexing of the diffraction patterns of the particles in the Nb-Mo-Al steel after TMP revealed the formation of (1) coarse Nb-rich carbides of predominantly cubic shape (Figure 5(a)); (2) fine spherical NbC particles, indicated by black arrows in Figure 5(a), with cubic lattice structure and lattice parameters of $a = b = c = 0.45$ nm (Figure 5(a)); (3) fine Mo-rich particles (MoC) indicated by white arrows in Figure 5(a) with hexagonal lattice structure and lattice parameters of $a = 1.06$ nm and $c = 1.34$ nm (Figures 5(a) and (c)); and (4) fine spherical Fe_3Nb_3C carbides with cubic lattice structure indicated by black arrows in Figure 5(b) and lattice parameters of $a = b = c = 1.13$ nm (Figures 5(b) and (d)). It could be suggested that the large Nb-rich carbides did not dissolve during austenitizing, whereas the fine Nb-rich and Mo-rich particles precipitated during TMP. The number density of particles in the Nb-Al steel was higher than in the Nb-Mo-Al steel after TMP. A significant increase in the number of fine precipitates was found in the Nb-Mo-Al steel after PS/BH (Table III). It is clear that as a result of PS/BH treatment, the bimodal distribution of sizes appeared in the Nb-Mo-Al steel: the first peak is associated with the fine ~14-nm-diameter particles, and the second peak for the coarser particles increased from a maximum diameter of ~23 nm in TMP condition to ~35 nm in PS/BH condition (Figure 4(b)).

D. *Atom Probe Tomography*

Analysis of matrix composition and particles was performed by APT. Volumes of the matrix that contained between 0.02 and 0.06, 0.1 and 0.25, and in excess of 2 at. pct C were deemed to be PF, BF, and M/RA, respectively. It is impossible to distinguish between M and RA in atom probe studies, as all RA appeared to transform to M at the temperature of the analysis. In addition, the PF was enriched in Si, whereas a lower than nominal Si content was measured in the BF. Detailed analysis for the TMP condition is given elsewhere.[27]

Table III. Particle Characterization and Precipitation Hardening Contribution for the Nb-Al and Nb-Al-Mo Steels After TMP and TMP/PS/BH Based on TEM Observations

Processing	TMP		TMP/PS/BH	
Steel	Nb-Al	Nb-Al-Mo	Nb-Al	Nb-Al-Mo
Total number of particles	66	56	65	69
Average particle size, equivalent diameter (nm)	14 ± 7	23 ± 7	29 ± 10	fine:14 ± 5 coarse: 35 ± 9
Particle density (N_v, m^{-3})	9.5×10^{20}	4.6×10^{20}	1.0×10^{20}	fine: 3.3×10^{22} coarse: 4.3×10^{20}
Contribution to the yield strength (MPa)	98 ± 38	94 ± 34	57 ± 18	178 ± 16

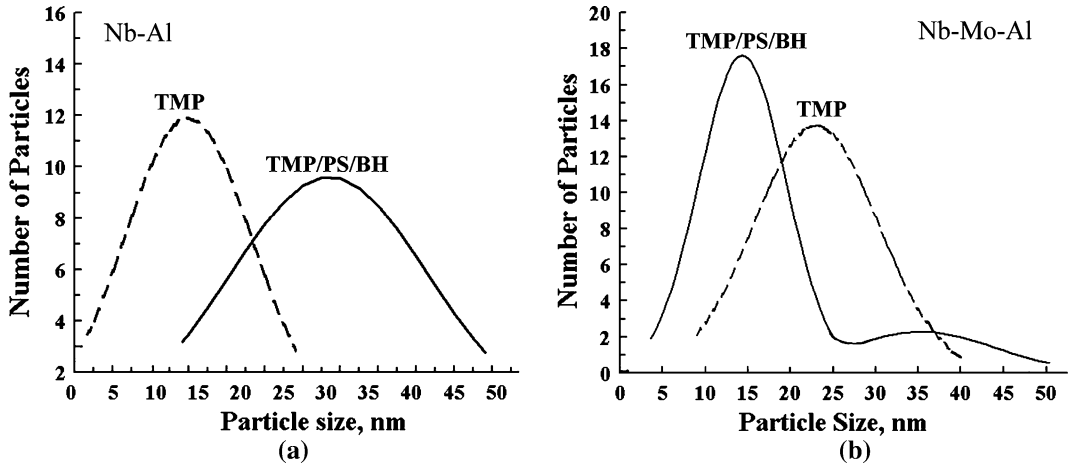

Fig. 4—Particle size distribution in the (*a*) Nb-Al steel and (*b*) Nb-Mo-Al steel after TMP and PS/BH.

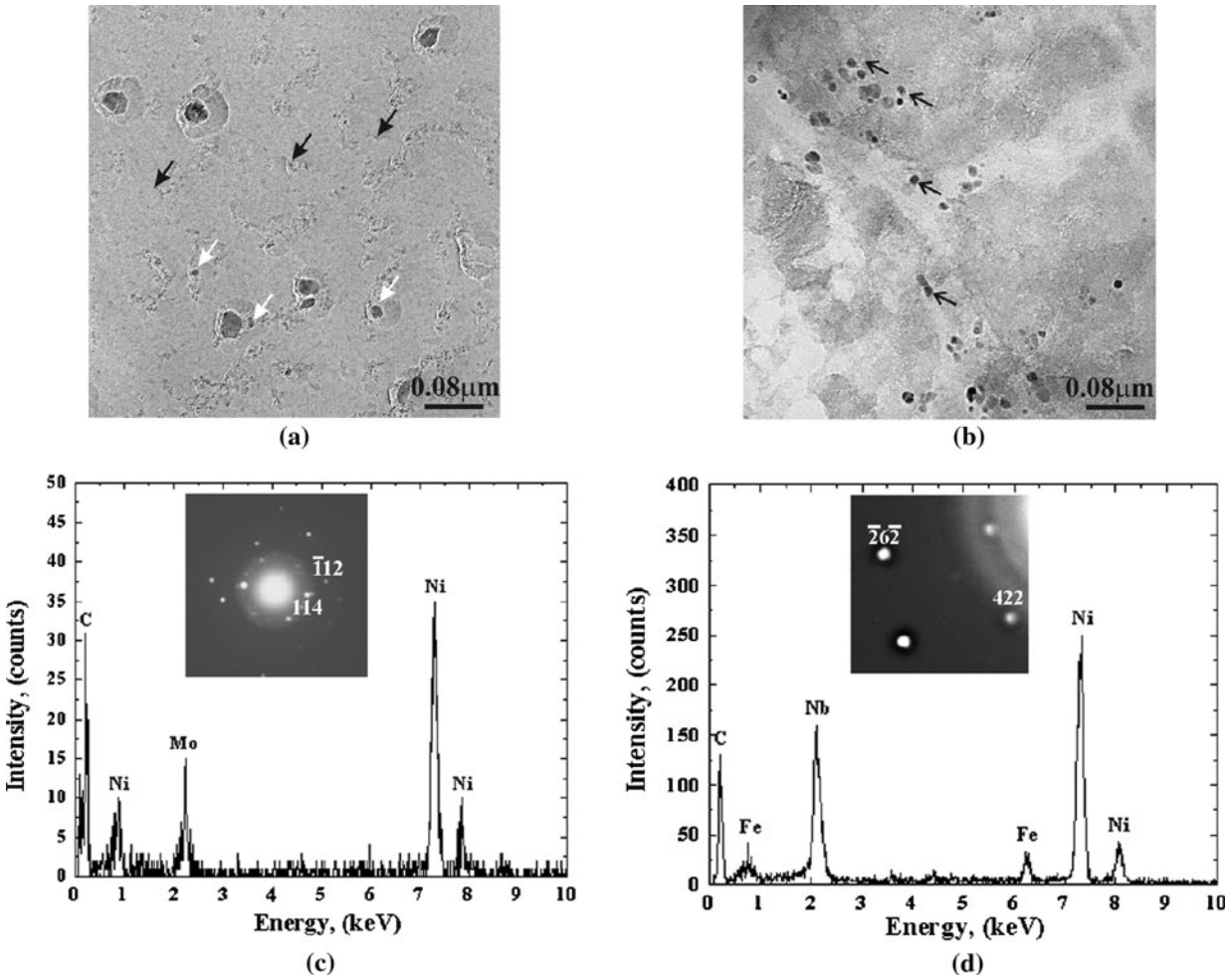

Fig. 5—(*a*) and (*b*) Carbon replicas from the Nb-Al-Mo samples after TMP showing (a) NbC (dark arrows) and MoC (white arrows), and (b) Fe_3Nb_3C (dark arrows). (*c*) Representative EDX spectrum and diffraction pattern with zone axis of $[\bar{1}31]$ (inset) from MoC carbides and (*d*) representative EDX spectrum and diffraction pattern with zone axis of $[\bar{4}17]$ (inset) from Fe_3Nb_3C carbides. The Ni peak is from the Ni grid.

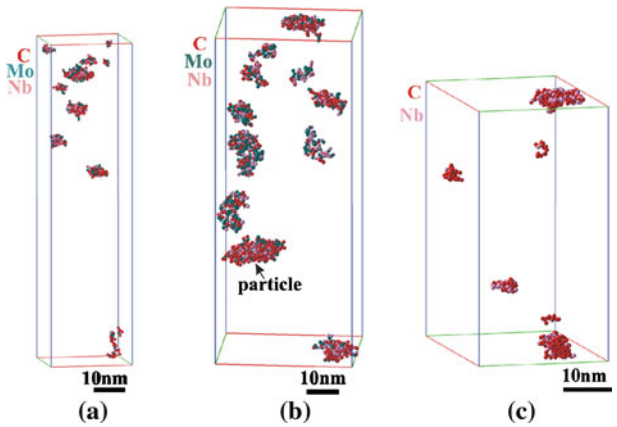

Fig. 6—Representative atom maps of clusters in the PF of (*a*) and (*b*) Nb-Al-Mo steel and (*c*) Nb-Al: (a) Nb-Al-Mo steel after TMP, (b) Nb-Al-Mo steel after PS/BH, and (c) Nb-Al steel after PS/BH. The matrix atoms were suppressed with the maximum separation method with $d_{max} = 1$ nm. (a) 9,081,297, (b) 5,059,784, and (c) 4,433,117 atoms in analyzed volumes.

The presence of nanoscale clusters and particles was detected in both steels after TMP and PS/BH. We considered clusters to be small segregations of solute atoms within the matrix phase with no clearly defined crystallographic structure. The Fe atom planes were clearly visible in the regions with clusters. On the other hand, precipitates detected by APT were much larger in size and had different crystallographic arrangements of atom planes from those in the matrix. However, the formation of *intermediate* nanoscale particles was found by APT. These particles showed all precipitate characteristics but had a size similar to that of the clusters and did not attain the equilibrium compositions. An example of clusters and particles in PF of the NbAlMo steel after TMP is shown in Figure 6(a), whereas their presence in PS/BH condition is shown in Figure 6(b). Clusters are relatively uniformly distributed within the matrix. Similarly, the presence of clusters and particles in PF of Nb-Al steel after TMP and PS/BH was also detected (Figure 6(c)). From the detailed analysis (Table IV and Figures 7 and 8), it is clear that there is a variation in cluster composition in both steels and conditions, with higher C content in clusters in the TMP condition than in the PS/BH one. The majority of clusters and fine precipitates in the Nb-Al-Mo steel after TMP had average composition of 64 ± 6 at. pct C, 16 ± 6 at. pct Mo, and 15 ± 5 at. pct Nb, whereas the average composition of

Table IV. Average Cluster Guinier Radius (r_G), Number Densities, and Cluster Hardening Contribution in the Steels as Estimated Using the Maximum Separation Method from Atom Probe Data

	Contribution to the Yield Strength (MPa)		Ferrite/B After TMP		Ferrite/B After PS/BH	
Steel	TMP	PS/BH	r_G (nm)	N_v (m^{-3})	r_G (nm)	N_v (m^{-3})
Nb-Al	24 ± 10	100 ± 31	2 to 5	0.6×10^{22}	1.5 to 5.5	4.9×10^{22}
Nb-Mo-Al	101 ± 30	126 ± 20	1.5 to 7.5	3.6×10^{22}	2 to 8	7.0×10^{23}

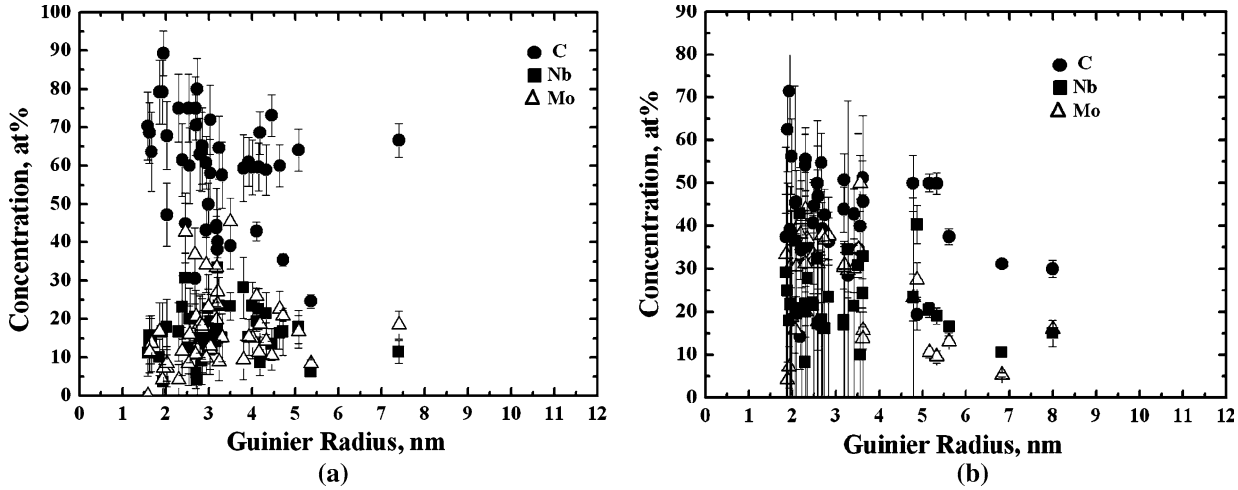

Fig. 7—Solute concentrations of the clusters and particles as a function of their Guinier radii found in the PF and BF of Nb-Al-Mo steel after (*a*) TMP and (*b*) PS/BH.

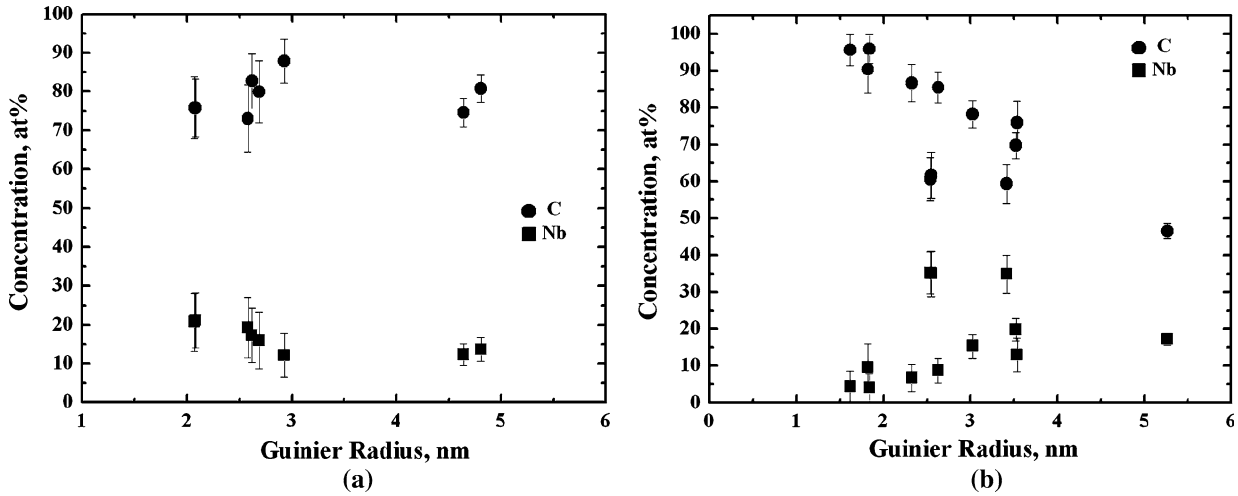

Fig. 8—Solute concentration of the clusters and particles as a function of their Guinier radii found in the PF and BF of Nb-Al steel after (*a*) TMP and (*b*) PS/BH.

majority clusters/fine precipitates after PS/BH was 46 ± 6 at. pct C, 28 ± 5 at. pct Mo, and 23 ± 4 at. pct Nb. The compositions of TMP clusters and fine particles are close to the composition of nonequilibrium $(MoNb)C_2$ carbides with cubic lattice structure and lattice parameters of $a = b = c = 0.44$ nm, whereas the composition of PS/BH clusters/fine precipitates was closer to the composition of nonequilibrium $C_{3.28}Mo_2Nb_2$ particles with cubic lattice and lattice parameters of $a = b = c = 0.43$ nm. However, the presence of equilibrium MoC carbides observed by TEM was also confirmed by APT. It appeared that, despite the low bake-hardening temperature, there is a diffusion of substitutional elements during bake hardening after PS in the Nb-Al-Mo steel.

The clusters and fine particles in ferrite/bainitic ferrite of Nb-Al steel after TMP with an average composition of 78.7 ± 6 at. pct C and 16.6 ± 4 at. pct Nb were

observed along with coarse NbC. The average composition of clusters and particles after PS/BH was 65 ± 3 at. pct C and 27 ± 5 at. pct Nb. These compositions are close to the composition of Nb_2C carbides with orthorhombic lattice structure and lattice parameters of a = 1.1 nm, b = 0.5 nm, and c = 0.3 nm. Moreover, as the size of clusters, *i.e.*, the Guinier radius, increases, the C content decreases, and the concentrations of Nb or Mo increase. The same trend of an increase in the Nb concentration in clusters/fine particles after PS/BH toward the equilibrium composition as in the Nb-Al-Mo steel was observed in the Nb-Al steel.

The number density of clusters was higher in PF/BF of Nb-Al-Mo than in the Nb-Al steel. It increased by an order of magnitude in Nb-Al-Mo steel, and to a lesser extent in Nb-Al steel, after PS/BH treatment. During BH, the coarsening of clusters in the Nb-Al-Mo steel was evident (Figure 7, Table IV) with the minimum average size increasing from 3.5 to 4 nm. In the Nb-Al steel, while slight coarsening took place, finer clusters than in TMP conditions were also detected. The presence of Fe_3C carbides in the PF/BF were confirmed for both steels.

Fine C-rich clusters were present in M/RA after TMP in both steels. The density of clusters in M of both steels in the TMP condition was an order of magnitude higher than that in PF/BF (Table IV). Clusters in M/RA with the Guinier radius ranging from 0.9 to 1 nm and from 0.9 to 1.4 nm were detected in Nb-Al and Nb-Al-Mo steel after TMP, respectively with the maximum separation method. The number density of clusters was $7.7 \pm 0.6 \times 10^{23}$ m^{-3} for Nb-Al steel and $3.1 \pm 0.3 \times 10^{23}$ m^{-3} for Nb-Al-Mo steel. During bake hardening, further decomposition of M took place (Figure 9) with simultaneous cluster formation and cluster growth. It resulted in the formation of fine rodlike Fe_3C carbides, oriented orthogonally to each other. These data are also collaborated by TEM observations of fine Fe_3C in both B and M in the steels after PS/BH. The maximum cluster size after PS/BH increased to 1.6 nm in the Nb-Al steel and to 4.8 nm in the Nb-Al-Mo steel. The number density of clusters and carbides after PS/BH was an order of magnitude higher than after TMP, which proves a continuous process of cluster formation during bake hardening. More detailed explanation on the decomposition of M during bake hardening is given elsewhere.[28]

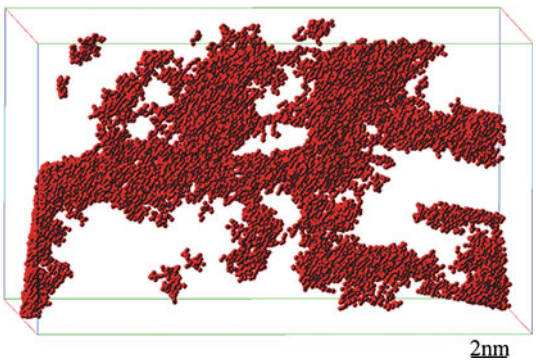

Fig. 9—Representative atom map showing the decomposition of M/RA in the Nb-Mo-Al steel after PS/BH. The matrix atoms were suppressed with the maximum separation method with d_{max} = 0.5 nm.

IV. DISCUSSION

A. *Understanding the Effect of PS/BH on the Microstructure*

TEM analysis of carbon replicas produced from both TRIP steel surfaces allowed the study of particle distribution and composition. The predominant carbides in the Nb-Al steel formed after TMP and PS/BH were NbC. Particle coarsening was evident after PS/BH of the Nb-Al specimen with the average particle diameter growing from ~14 to 29 nm (Table III). Overall, particle density remained relatively unchanged after PS/BH treatments of the Nb-Al steel (Table III). In contrast, PS/BH in the Nb-Mo-Al led to the nucleation of new fine particles in addition to coarsening of pre-existing particles. The addition of Mo increased the tendency of particles formation with various compositions. On average, particles in the original TMP microstructure of the Nb-Al-Mo steel coarsened from ~23 to 35 nm during the subsequent treatments. This was accompanied by the increase in overall particle density by at least an order of magnitude. However, it was suggested that the coarsening of the fine particles was accompanied by reduction in their carbon content toward more equilibrium phases. It is likely that these fine particles are precursors for the equilibrium precipitates such as NbC or Mo_2C.

APT work revealed a relatively uniform distribution of diffuse clusters and nanoscale particles before and after PS/BH in the PF and bainitic ferrite of both steels. Importantly, overall cluster density increased by an order of magnitude after the PS/BH treatment of Nb-Al-Mo steel. This would lead to enhanced dislocation and cluster interactions and suggests an additional explanation for the improved strength of this steel after the treatments. The Nb concentrations in the larger clusters after PS/BH also appear to have increased. Although cluster size stayed relatively unchanged in the Nb-Al steel during PS/BH treatments, the spacing reduced marginally also leading to increased cluster density in the Nb-Al specimen.

An increase in clusters and particle size and formation of new clusters and nanoscale precipitates at sufficiently low BH temperature could be explained by the heterogenous nucleation of clusters and nanoscale precipitates on dislocations or along grain boundary and enhanced growth due to the pipe diffusion through dislocations or due to a rapid diffusion along the grain boundary. The high dislocation density of bainitic ferrite and an increase in dislocation density of ferrite/bainitic ferrite as a result of PS for both steels allowed consideration of the pipe diffusion of Nb and Mo along dislocation cores, which increases the coarsening rate of the precipitates.[28,29] The presence of a high number of dislocations also causes a significant acceleration in nucleation of new clusters and precipitates.[30]

The APT data were used to calculate the distance that Nb atoms in the Nb-Al steel can diffuse along the dislocation at BH temperature 453 K (180 °C) after PS. The concentration of Nb in the cluster/precipitate (X_{Nb}) was calculated using the following equation:[31]

$$X_{Nb} = \frac{4}{3}\pi r_G^3 \times n_c \times x_{Nb} \quad [2]$$

where r_G is the Guinier radius of clusters in the Nb-Al steel after PS/BH (1.5 to 5.5 nm) (Table IV), n_c is the number density of the clusters (4.9×10^{22} m^{-3}) (Table IV), and x_{Nb} is the concentration of Nb in clusters calculated from APT data (Figure 8) (8 to 22 at. pct). The value of x_{Nb} was calculated to be 0.0055 to 0.0152 at. pct, which correlates with the amount of Nb in the bulk composition (Table I).

The size of the diffusion cell (r_d), *i.e.*, the volume of the matrix, which can supply the formation of one Nb cluster, was determined from the following equation:

$$\frac{4}{3}\pi(r_d)^3 X'_{Nb} = \frac{4}{3}\pi(r_G)^3 X_{Nb}, \text{ or } r_d = 7.9 r_G \quad [3]$$

where x'_{Nb} is the amount of Nb in the steel (Table I) and x_{Nb} is the Nb concentration in the cluster. The size of the diffusion cell for a 1.5-nm-diameter Nb cluster was 11.9 nm, and for a cluster size of 5.5 nm, it was 43.5 nm.

The next step was the calculation of the diffusion coefficients in order to define the possibility of Nb atoms diffusing over the distance r_d during BH. The self-diffusion coefficient of Fe in ferrite could be calculated as[31]

$$D_{Fe}^{\alpha(ferro)} = 0.5 \exp\left(-\frac{Q}{RT}\right) \text{cm}^2/\text{s} \quad [4]$$

where Q is the activation energy (240,000 J mol^{-1}), R is the universal gas constant, and T is the temperature of interest (Kelvin). Assuming that the activation energy of pipe diffusion is $0.7 \times Q$ and that the Nb diffusivity is within a factor of ~5 from the self-diffusivity of Fe,[30] the diffusion coefficient for pipe diffusion was

$$D_{Nb}^{\alpha(pipe)} \approx 0.5 \exp\left(-\frac{168,000}{R \cdot 453}\right) = 2.1 \times 10^{-20} \text{cm}^2/\text{s} \quad [5]$$

The extent of pipe diffusion over a distance was given by

$$x = \sqrt{q D_{Nb}^{\alpha(pipe)} t} \quad [6]$$

where t is the time of BH (1800 seconds). The distance is calculated to be 0.06 nm. Taking into account the volumes that were obtained for r_d, it appeared that Nb atoms did not have time to form a cluster at this temperature.

Another possibility to form a cluster at BH temperature is diffusion of Nb along the grain boundary. In this case, the boundary thickness δ is assumed to be 5×10^{-8} cm:[31]

$$D_{Nb}^{\alpha(boundary)} \approx \exp\left(-\frac{155,000}{R \cdot 453}\right) = 1.3 \times 10^{-18} \text{cm}^2/\text{s} \quad [7]$$

where $D_{Nb}^{\alpha(boundary)}$ is the diffusion coefficient for diffusion along the grain boundary. The diffusion distance along the grain boundary was calculated to be 0.48 nm. This number is still low and there was no time for Nb to diffuse along the grain boundary and form clusters.

However, it was reported by Gjostein[32] that at low temperatures, the surface diffusivity becomes larger by a few orders of magnitude than that predicted from a simple Arrhenius plot[32] for high-temperature diffusivity. The slop of the Arrhenius plot of surface diffusivity decreased considerably (to ~1/2.5) below ~$0.75T_M$ (T_M is the melting temperature) from the value at temperatures higher than that, although the mechanism for the variation of the activation energy was not identified. Data on the diffusion along the grain boundary or dislocation at low temperatures are scarce. Accordingly, the activation energy of Nb or Mo diffusion, which yields diffusion distances comparable to r_d, was calculated and the result was $0.52 \times Q$ to obtain r_d (28 nm). In view of the fact that the atom migration energy is ~$0.4 \times Q$ for volume diffusion,[33] the decrease in the activation energy from $0.7 \times Q$ for pipe diffusion and $0.65 \times Q$ for boundary diffusion to ~$0.5 \times Q$ at very low temperature ($T/T_M < 0.3$), and thus the possibility that Nb atoms have time to diffuse over the interparticle distance during BH of the prestrained Nb-Al and Nb-Al-Mo steels, does not seem to be unexpected.

APT work provided no evidence on atomic atmosphere formation around dislocations for either steel after PS/BH, as suggested by strain-aging theory. Therefore, the proposed Cottrell atmosphere strengthening mechanism reported in Reference 34 was not observed for the steels analyzed. It appeared that the interaction energy between the Nb and Mo carbides and carbon atoms was greater than that between the dislocations and the carbon atoms. The binding energy of carbon to dislocations is ~ 0.75 eV,[34] while the binding energy of carbon to NbC carbides is ~2.3 eV.[35] For both steels here, it can be proposed that carbon atoms were more likely to diffuse to form nanoscale particles than they were to diffuse to dislocations.

APT also revealed the presence of fine C-rich clusters in the M of both steels after TMP. These could be formed during cooling from the coiling temperature or during autotempering at room temperature. More detailed characterization was given elsewhere.[35] Formation of Fe-C carbides as a result of M decomposition was observed in both steels after PS/BH. This was a continuous process starting from the formation of C clusters as precursors to carbide formation, followed by a compositional evolution and increase in size of carbides.[35]

B. *Contribution of Precipitation and Cluster Strengthening to the Yield Strength Increase*

The contribution of precipitation hardening to the yield strength before and after PS/BH was studied for both steels. The PS/BH of both steels provided a high increase in the yield strength and a decrease in elongation (Table II). The bainitic ferrite laths were more refined in the Nb-Al-Mo steel than in the Nb-Al steel. The bainitic ferrite laths refinement and Mo strengthening effect could be the reasons for the additional strengthening observed in the Nb-Al-Mo steel compared to the Nb-Al steel (Table II).

From TEM data on the particle characterization, the contribution of particles found in the bainitic ferrite/PF to an increase in the yield strength of both steels was calculated from the Ashby–Orowan relationship:[36]

$$\Delta\tau_y = 0.84\left(\frac{1.2G\mathbf{b}}{2\pi L}\right)\ln\left(\frac{d}{2\mathbf{b}}\right) \quad [8]$$

where G is the shear modulus (80 GPa), $\mathbf{b}$ (meters) is the Burger's vector (0.25 nm), L (meters) is the distance between particles, and d (meters) is the diameter of particles. It was also assumed that the particles are hard spheres and are not sheared by dislocations during plastic deformation. The errors associated with these calculations deemed to be large owing to significant uncertainty surrounding the separation distance of particles. It may also be possible that the images analyzed were of regions that contained higher than average particle density. Taking into account that the total amount of ferrite and B is ~80 pct for both steels, the increase in the yield strength due to the precipitation hardening in the Nb-Al steel was estimated to be 98 ± 38 after TMP and 57 ± 18 MPa after TMP/PS/BH, while an increase in the yield strength in the Nb-Al-Mo steel was 94 ± 34 after TMP and 178 ± 16 MPa after TMP/PS/BH (Table III). The contribution of particles to an increase in the yield strength after PS/BH of Nb-Al-Mo steel was higher than in the Nb-Al steel. It correlates with tensile testing results and BH response values, as the higher yield strength and BH response were found in the Nb-Al-Mo steel after PS/BH than in the Nb-Al steel (Table II).

From APT data, it is possible to calculate an additional contribution of clusters and intermediate particles to an increase in yield strength of both steels. For the clusters and intermediate particles, which were uniformly distributed in the ferrite/bainitic ferrite matrix, the Ashby–Orowan mechanism could not be used, since this mechanism assumes the random dispersion of hard, incoherent precipitates on a slip plane and dislocation bowing around them.[36] Moreover, it could be assumed that the clusters/intermediate precipitates are coherent with the matrix phase and the dislocations shear the clusters during deformation, as was observed for the GP zones in Al alloy. It has been proposed[37,38] that the precipitation strengthening effect of fine clusters can be calculated from

$$\Delta\sigma = \frac{K}{d}f^{1/2}\ln\frac{d}{\mathbf{b}} \quad [9]$$

where K is a constant (5.9 N/m), $\mathbf{b}$ is the Burger's vector, f is the volume fraction of particles (pct) calculated from APT data, and d is the diameter of fine precipitates measured by APT. The contribution of clusters/intermediate particles to an increase in yield strength was 24 ± 10 and 101 ± 30 MPa after TMP for the Nb-Al and Nb-Al-Mo steel, respectively, and 100 ± 31 and 126 ± 20 MPa after PS/BH for the Nb-Al and Nb-Al-Mo, respectively (Table IV). From all the conditions studied, the highest total contribution of coarse particles and clusters/intermediate precipitate to the yield strength (304 MPa) was found in the Nb-Al-Mo steel after PS/BH, while the lowest was in the Nb-Al steel after TMP (194 MPa). Although the BH responses observed in both steels could not be fully accounted for by considering only precipitation and cluster strengthening mechanisms, as there also will be contributions from the increase in dislocation density from PS leading to the corresponding increases in work hardening and solid solution strengthening, fine particles/clusters play a major role in the yield strength increase after PS/BH treatment.

V. CONCLUSIONS

The microstructure-property relationship in two C-Mn-Si-Nb-Al-(Mo) thermomechanically processed TRIP steels before and after PS/BH treatment was studied. The formation of two types of particles was observed in both steels before and after PS/BH treatment using TEM and APT: (1) coarse equilibrium Nb-C and Nb-Mo-C precipitates formed during initial processing or TMP; and (2) intermediate nanoscale Nb-C and Nb-Mo-C particles and clusters formed during TMP or during BH. Moreover, the PS/BH treatment led to an increase in the number density of particles and clusters for both steels. It was suggested that these changes could be explained by the diffusion of Nb and Mo at BH temperature, if it is assumed that, similar to the surface diffusivity, their diffusivity changes with temperature differently from the one extrapolated based on the Arrhenius plot. From TEM and APT data on the particles and clusters, the estimation of their contribution to the yield strength before and after PS/BH was performed. The highest contribution of particles and clusters to the yield strength (304 MPa) was found in the Nb-Al-Mo steel after PS/BH.

ACKNOWLEDGMENTS

The authors thank K.F. Russell, Oak Ridge National Laboratory, for technical assistance. Atom probe research at the Oak Ridge National Laboratory SHaRE User Facility was sponsored by the Scientific User Facilities Division, Basic Energy Sciences, United States Department of Energy.

REFERENCES

1. Y. Sakuma, O. Matsumura, and H. Takechi: *Metall. Trans. A*, 1991, vol. 22A, pp. 489–98.
2. H.K.D.H. Bhadeshia and D. Edmonds: *Metall. Trans. A*, 1979, vol. 10A, pp. 1895–907.
3. M.D Meyer, D. Vanderschueren, and B.C. De Cooman: *ISIJ Int.*, 1999, vol. 39 (8), pp. 813–22.
4. M.G. Akben, B. Bacroix, and J.J. Jonas: *Acta Metall.*, 1983, vol. 31, pp. 161–74.
5. H.C. Chen, H. Era, and M. Shimizu: *Metall. Trans. A*, 1989, vol. 20A, pp. 437–45.
6. K. Hulka: *Mater. Sci. Forum,* 2005, vols. 473–474, pp. 91–102.
7. W. Bleck, A. Frehn, E. Kechagias, J. Ohlert, and K. Hulka: *Mater. Sci. Forum*, 2003, vols. 426–432, pp. 43–48.
8. M. Bouet, J. Root, E. Es-Sadiqi, and S. Yue: *Mater. Sci. Forum*, 1998, vols. 284–286, pp. 319–26.
9. S. Hashimoto, S. Ikeda, K. Sugimoto, and S. Miyake: *ISIJ Int.*, 2004, vol. 44, pp. 1590–97.

10. P.J. Jacques, J. Ladrière, and F. Delanny: *Metall. Mater. Trans. A*, 2001, vol. 32A, pp. 2759–68.
11. E. Jimenez-Melero, N.H. van Dijk, L. Zhao, J. Sietsma, S.E. Offerman, J.P. Wright, and S. van Zwaag: *Acta Mater*, 2007, vol. 55, pp. 6713–23.
12. M.D. Meyer, D. Vanderschueren, and B.C. De Cooman: *ISIJ Int*, 1999, vol. 39, pp. 813–22.
13. L.J. Baker, S.R. Daniel, and J.D. Parker: *Mater. Sci. Technol.*, 2002, vol. 18, pp. 355–68.
14. A.H. Cottrell and B.A. Bilby: *Proc. Phys. Soc.*, 1949, vol. 63, pp. 49–62.
15. M. Kinoshita and A. Nishimoto: *CAMP-ISIJ*, 1990, vol. 3, pp. 1780–85.
16. B.C. De Cooman: *Curr. Opin. Solid State Mater. Sci*, 2004, vol. 8, pp. 285–303.
17. I.B. Timokhina, E.V. Pereloma, and P.D. Hodgson: *Metall. Mater. Trans. A*, 2007, vol. 38A, pp. 2442–50.
18. I.B. Timokhina, E.V. Pereloma, and P.D. Hodgson: *Mater. Sci. Forum*, 2007, vols. 539–547, pp. 4315–20.
19. I.B. Timokhina, M. Ryan, M.K. Miller, and E.V. Pereloma: *Iron Steel*, 2005, vol. 40, pp. 744–48.
20. "Metals Test Methods and Analytical Procedures," *Annual Book of ASTM Standards*, 1993, 03.01(E 8), p. 130.
21. T. Waterschoot, A.K. De, S. Vandeputte, and B.C. De Cooman: *Metall. Mater. Trans. A*, 2003, vol. 34A, pp. 781–91.
22. B.D. Cullity: *Elements of X-Ray Diffraction*, Addison-Wesley Publishing Company, Boston, MA, 1978, p. 555.
23. I.B. Timokhina, P.D. Hodgson, and E.V. Pereloma: *Metall. Mater. Trans. A*, 2003, vol. 34A, pp. 1599–1609.
24. P.B. Hirsch, R.B. Nicholson, A. Howie, D.W. Pashley, and M.J. Whelan: *Electron Microscopy of Thin Crystals*, Butterworth and Co., London, 1965, p. 51.
25. M.K. Miller: *Atom Probe Tomography*, Kluwer Academic Press, New York, NY, 2005, pp. 188–89.
26. I.B. Timokhina, P.D. Hodgson, and E.V. Pereloma: *Metall. Mater. Trans. A*, 2004, vol. 35A, pp. 2331–41.
27. E.V. Pereloma, I.B. Timokhina, M.K. Miller, and P.D. Hodgson: *Acta Mater.*, 2007, vol. 55, pp. 2587–98.
28. E.V. Pereloma, M.K. Miller, and I.B. Timokhina: *Metall. Mater. Trans. A*, 2008, vol. 39A, pp. 3210–16.
29. S. Spigarelli, E. Cerri, P. Bianchi, and E. Evangelista: *Mater. Sci. Technol.*, 1999, vol. 15, pp. 1433–40.
30. B. Dutta, E.J. Palmiere, and C.M. Sellars: *Acta Mater.*, 2001, vol. 49, pp. 785–94.
31. J. Fridberg, L.E. Torndahl, and M. Hillert: *Jernkontorets Annaler*, 1969, vol. 153 (6), pp. 263–76.
32. N.A. Gjostein: *Met. Surf. ASM,* 1963, pp. 99–103.
33. P. Shewmon: *Diffusion is Solids*, 2nd ed., TMS, Warrendale, PA, 1989, pp. 78–89.
34. A.W. Cochardt, G. Schoek, and H. Wiedersich: *Acta Mater.*, 1955, vol. 3, pp. 533–37.
35. E.V. Pereloma, K.F. Russell, M.K. Miller, and I.B. Timokhina: *Scripta Mater.*, 2008, vol. 58, pp. 1078–81.
36. T. Gladman: *Mater. Sci. Technol.*, 1999, vol. 15, pp. 30–36.
37. H.J. Kestenbach, S.S. Campos, and E.V. Morales: *Mater. Sci. Technol.*, 2006, vol. 22, pp. 615–26.
38. D. Kalish and M. Cohen: *Mater. Sci. Eng.*, 1970, vol. 6, pp. 156–66.